

Studies on $\text{Bi}_2\text{Fe}_4\text{O}_9$ Ceramic

4. Introduction

Photocatalyst with higher activities for the environmental applications i.e. water disinfection, water purification, air purification has been major challenges in the recent years. Among them, photocatalysis based on semiconductor such as titanium oxide has been attracted towards more attention for environmental applications due to strong oxidizing power, good chemical inertness, long-term stability and cost effectiveness etc. [1]–[3]. With dielectric constant, It has been used as a green technique for air and water treatment. Definitely, TiO_2 is certainly an excellent photocatalyst that carries out aerophilous decomposition. There are many organic compounds under UV radiation, whose band gap (3.2) is higher than TiO_2 , which limits any application [2], [4], [5]. Over many years, a number of photocatalytic semiconductors were worked out, such as $\text{CaBi}_{12}\text{O}_4$, BiFeO_3 , SrTiO_3 - Fe_2O_3 , and the metallic element WO_{12} , in addition to which a rumor has been reported [6], [7]. The band gap of those metal oxide which are applicable for the absorption of light, so that could doubtless be economical photocatalysts beneath light. $\text{Bi}_2\text{Fe}_4\text{O}_9$ is a crucial material that may be used as a semiconductor gas sensing element and catalyst for ammonia oxidization. Beside the above named application, a recently study has been reported to $\text{Bi}_2\text{Fe}_4\text{O}_9$ material that may be used as a semiconductor gas identifying element and catalyst for ammonia oxidation. Furthermore, $\text{Bi}_2\text{Fe}_4\text{O}_9$ nanoplates will act as photocatalysts for acid-base indicator (MO) degradation below visible light irradiation, whereas the $\text{Bi}_2\text{Fe}_4\text{O}_9$

microplates solely exhibit this performed below ultraviolet light. Bi₂Fe₄O₉ as a specific type of photocatalytic under UV- Visible light and it is used as semiconducting material, a possible gas sensitive material and catalyst for ammonia chemical reaction to NO [8], [9]. The microstructural property play important role in determine the physical properties of crystal. The magnetic property, optical property, and semiconductor properties are closely related to their morphology [10], [11]. In addition to this, the relationship between the photocatalytic property and the electronic structure should also been studied to guide the further improvement of the photocatalytic activity. Moreover, investigations on photocatalytic performance only by photodegradation of dyes are not convincing, as it is hard to avoid the discoloring of dyes from adsorption and photosensitization. Photodegradation experiments on alternative organic contaminants are necessary to any judge the photocatalytic performance and create preparations for its practical applications within the future. Liquid ammonia together of the most important nitrogen-containing pollutants in waste may be a potential supply of oxygen depletion thanks to eutrophication. [7] Both ammonium ion NH₄⁺ and its conjugate base NH₃ are often present in water and effluent. Though the photocatalytic oxidation of NH₄⁺ /NH₃ by TiO₂ has been reportable in many studies, there are few reports on the photodegradation of NH₄⁺ /NH₃ in alternative systems. It's revealing to begin the studies on the NH₄⁺ /NH₃ degradation by alternative photocatalysts, such as the ready Bi₂Fe₄O₉ underneath actinic ray irradiation. Besides NH₄⁺ /NH₃, the photocatalytic degradation of phenol on Bi₂Fe₄O₉ is also according within the present paper. As is renowned, phenol is a wide used organic chemical present during a sort of wastewaters from numerous completely different industries, and it's quite toxic and slowly degradable within the atmosphere. The phenol removal is additionally of high

environmental concern to seek out a good photocatalyst for its oxidization. [8] Bi₂Fe₄O₉, an antiferromagnetic semiconductor with a mullite structure has attracted in depth interest for its specific magnetic structures, potential photocatalytic application beneath ultraviolet (UV) and visual light, and distinctive role as a gas sensor. The crystallographic structure of Bi₂Fe₄O₉ belongs to the orthorhombic space cluster Pbam, whose building block consisting of two formula units are often delineated as columns of edge-sharing FeO₆ octahedral connected by corner sharing FeO₄ tetrahedral and bismuth atoms. [[10]] Although the antimagnetic force structure of Bi₂Fe₄O₉ has been investigated by many teams, the size dependent magnetic properties of Bi₂Fe₄O₉ Cs haven't been reported nevertheless, and also the investigation into the dimensions dependence of magnetic properties is of Brobdingnagian importance for elementary researches and applications in spintronics. Bi₂Fe₄O₉ NCs exhibit wonderful photocatalytic reaction of stain (MB) below actinic ray irradiation with the help of a little amount of H₂O₂. It's conjointly found that a metamorphosis from antiferromagnetism to weak magnetic force happens once the average diameter of the nanoparticles is below 57 nm, and smaller Bi₂Fe₄O₉ NCs exhibit higher photocatalytic activity under visible-light irradiation. Moreover, at the same time, our samples show quicker degradation rate below actinic ray irradiance with the help of H₂O₂ than do microplatets and nanosheets prepared by Ruan and Zhang. [11] Bi₂Fe₄O₉ is also attention-grabbing because of its multiferroic nature, high gas sensitivity, and chemical action oxidisation of ammonia to NO. The creation of nanostructures could be a basic strategy to realize excellent photocatalytic activity since the photocatalytic reaction occurs dominantly on the catalyst surface and nanostructures can without doubt offer an oversized expanse to volume magnitude relation. Up to now, the preparation

of nanostructured Bi₂Fe₄O₉ has been chiefly based on the hydrothermal method, sol-gel template technique, and melted salt technique. Within the side of morphology management, the hydrothermal route offers a plus over alternative preparation techniques; but, the merchandise obtained from the tactic tend to possess a reasonably massive particle size, and furthermore a cumbersome abstersion method is usually needed to clean out impurities. The properties of useful materials powerfully rely on their morphology, microstructure, dimension and crystallinity. Manageable microstructure and morphology area unit vital not just for basic analysis but additionally for technological applications. For the sake of morphology control, various methods such as hydrothermal process, sol-gel, solid state reaction, and molten-salt synthesis for the preparation of Bi₂Fe₄O₉ have been employed [12]–[14].

In the present study, Bi₂Fe₄O₉ ceramic was synthesized by the chemical method for improvement of photocatalytic activity of the materials as chemical route is the one of foremost promising routes than other route due to its low cost, simple process, and low reaction temperature, potential price and advantage for large –scale production.[6].

2. Experimental details

2.1. Material Synthesis

Analytical grade chemicals, Bi(NO₃)₂.6H₂O (99% Merck, India) and iron nitrate Fe (NO₃)₃.9H₂O were taken as starting materials for the synthesis of Bi₂Fe₄O₉ ceramic by the chemical route. The stoichiometric amount of bismuth nitrates was dissolved in de-ionized distilled water along with appropriate amount of glycine (C₂H₅ (NO₂), 99% Merck, India) as per equivalent to the metal ions. The resulting reaction mixtures were heated on a hot plate magnetic stirrer and maintaining the temperature 70 – 80 °C for evaporation of excesses of water. A fluffy mass obtained in the ignition process which

burnt with a sooty flame. The obtained fluffy mass was crushed into fine powder with the help of mortar and pestle. The resultant dry powder was calcined at 600 °C for 6 h in the electrical muffle furnace and made pellets (13.0 mm diameters, 1.6 mm thicknesses) using 2 wt% polyvinyl alcohol (PVA) as a binder. These pellets were sintered at 800 °C for 6 h and further carried out different types of physiochemical characterizations such as XRD, SEM, TEM, EDX, Cyclic voltammetry, and Photocatalytic activity.

A Congo red (CR) dye was selected as the model pollutant in the adsorption study. Initially, a 500 mg/L of CR stock solution was prepared, and experimental samples of respective concentrations (5, 10, 20, 30, 40, and 50 mg/L) were prepared by serial dilution technique. A standard curve of CR was prepared at 497 nm by using a UV–vis spectrophotometer (Universal Bio, India). The batch adsorption study was performed in 100 mL Erlenmeyer flask by adding adsorbent into 50 mL CR solution and shaken at 120 rpm and 30 ± 1 °C. The effect of process time (0.5-10 min), CR concentration (5-50 mg/L), and adsorbent dosage (0.1-1.0 g/L) were studied against the removal of CR. The samples were taken at regular time intervals and then centrifuged at 5000 rpm for 5 to measure the final CR concentration. The removal efficiency (%) and adsorption capacity (q_e (mg/g)) of CR dye was measured by the following equations.

$$\text{Removal efficiency of CR dye} = \frac{(C_{in} - C_{out})}{C_{in}} \times 100 \quad (1)$$

$$\text{Adsorption capacity } (q_e) = \frac{(C_{in} - C_{out})}{M} \times V \quad (2)$$

where C_{in} and C_{out} represent the inlet and outlet concentration of CR dye (mg/L), respectively. V is the volume of CR solution (L) and M is the mass of adsorbent (mg/g).

2.2. Material characterization

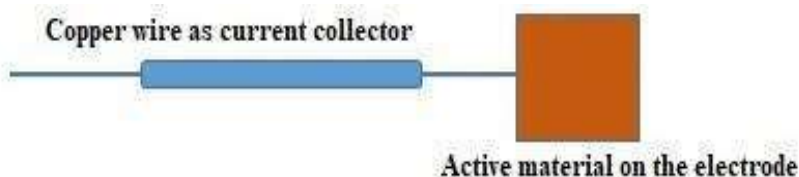
The crystalline phase of sintered material was identified by an X-rays Diffractometer (Rigakuminiflex 600, Japan) at a scan rate of 3°/min in 2θ range of 20-80° employing CuK_α radiation of wavelength, $\lambda=1.54059 \text{ \AA}$. The morphology of the fractured surface of sintered Bi₂Fe₄O₉ was characterized by scanning electron microscope (ZEISS, model EVO-18 research; Germany). The Bright field TEM images were obtained with the help transmission electron microscopy (TEM, FEI Tecnai-20G²) with an accelerating voltage of 200kV. For dielectric measurements, the pellets were polished and painted by silver paste; then dried at 300 °C for 3h to form electrodes for the respective characterizations. Electrical measurement data were taken by LCR meter (PSM1735-NumtriQ, Newton 4th Ltd UK) by varying the temperature and frequency. Optical band gap energy of Bi₂Fe₄O₉ nanoparticle was evaluated from the observed diffuse reflectance spectra. Reflectance spectra recorded with the help of balanced deuterium-halogen source (DH 2000 BAL, Ocean Optics) with 210-2500 nm spectral range.

Electrochemical characterizations:

Cyclic voltammetry and electrochemical impedance spectroscopy of all the samples have been performed by Versa STAT 3. Corresponding details have been studied in our earlier research work [15], [16].

Electrode preparation:

The electrode preparation methods have been discussed in our earlier paper [17], [18].



Results and discussion

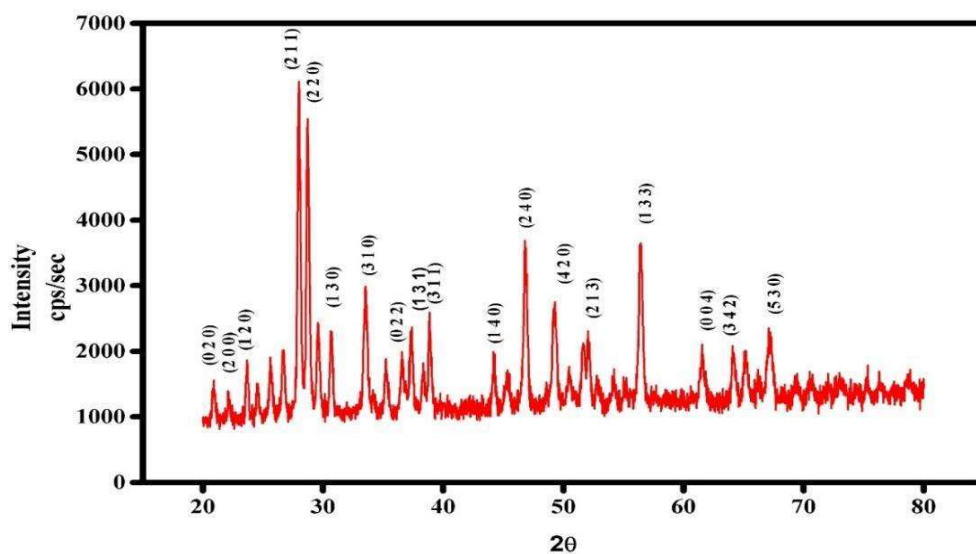


Figure 1. X-ray diffraction (XRD) pattern of $\text{Bi}_2\text{Fe}_4\text{O}_9$ ceramic sintered at 800°C for 8 h

X-ray diffraction pattern of $\text{Bi}_2\text{Fe}_4\text{O}_9$ polycrystalline ceramic sintered at 800°C for 8 h is shown in **Figure 1** which confirms the single phase formation of the materials. All the diffraction peaks are correctly matched with JCPDS card no. 20-0836 which clearly reveals the absence of secondary phases in the synthesized materials. The orthorhombic structure of $\text{Bi}_2\text{Fe}_4\text{O}_9$ ceramic was fabricated by two formula units per unit cell. These formula units consist of evenly distributed FeO_6 octahedrons and FeO_4 tetrahedrons with a lower packing density than that of corresponding closed packed structures. The Bi^{3+} ions are surrounded by eight oxygen ions with mutually orthogonal shorter BiO_3 and longer BiO_5 units. The most intense peaks of $\text{Bi}_2\text{Fe}_4\text{O}_9$ ceramic

corresponding to the planes (211), (220), (240), (133), (310), (420), (213), (530) are observed in the XRD pattern. All the characteristic peaks of XRD data were indexed on the basis of a cubic unit cell similar to Bi₂Fe₄O₉. The lattice parameter and unit cell volume of Bi₂Fe₄O₉ ceramic were determined by using “Cel” software having lattice parameter a=7.97 Å, b=8.43 Å, c = 6.01Å. The crystallite size (D) of Bi₂Fe₄O₉ ceramic was calculated with the help of Debye–Scherer’s formula as given by the following expression.

$$D = k\lambda/\beta \cos \theta \quad (3)$$

where, k is a dimensionless shape factor, with a value taken as 0.90, λ is the wavelength of X-ray, θ is the diffraction angle (Bragg angle), and β is the peak width of the diffraction peak at half-maxima (FWHM) and their value is taken as in radian. The β is corrected value of diffraction peak due to instrumental broadening for crystallite size with reference to standard silicon wafer sample. The average crystallite size of Bi₂Fe₄O₉ ceramic calculated by Debye–Scherer’s formula and found to be 37.71 nm.

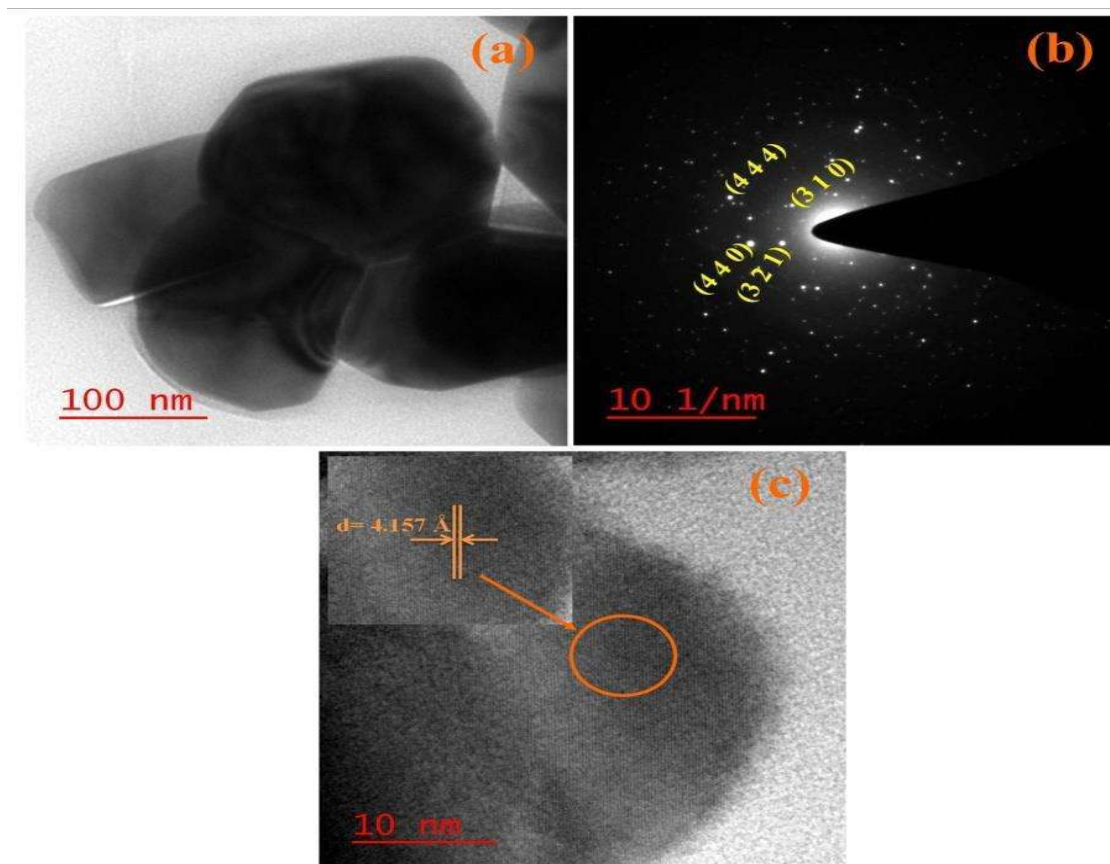


Figure 2. Represent bright field TEM image (b) indicate SAED pattern (c) HR -TEM images of Bi₂Fe₄O₉ ceramic sintered at 800°C for 8 h

Bright field TEM images of Bi₂Fe₄O₉ ceramic sintered at 800 °C for 8 h is depicts in **Figure 2(a)** which reveals the presence of bimodal shape of the particles. The average particles size of Bi₂Fe₄O₉ ceramic was found to be 102.58 nm. Bright spot pattern observed in selected area diffraction (SAED) patterns for Bi₂Fe₄O₉ ceramic shown in Fig. 2(b), emerging through the corresponding planes (4 4 4), (3 1 0), (4 4 0) and (3 2 1), respectively confirmed crystalline nature of the material. **Figure 2(c)** exhibits high resolution TEM image displaying inter-planar (d) spacing for Bi₂Fe₄O₉ ceramic. The d-spacing value observed for the Bi₂Fe₄O₉ ceramic is $d = 4.157 \text{ \AA}$ with the corresponding

plane (2 1 1). The entire diffraction pattern obtained in the SAED pattern and HR-TEM image are good agreements with the JCPDS card number 46-0416 of the XRD results.

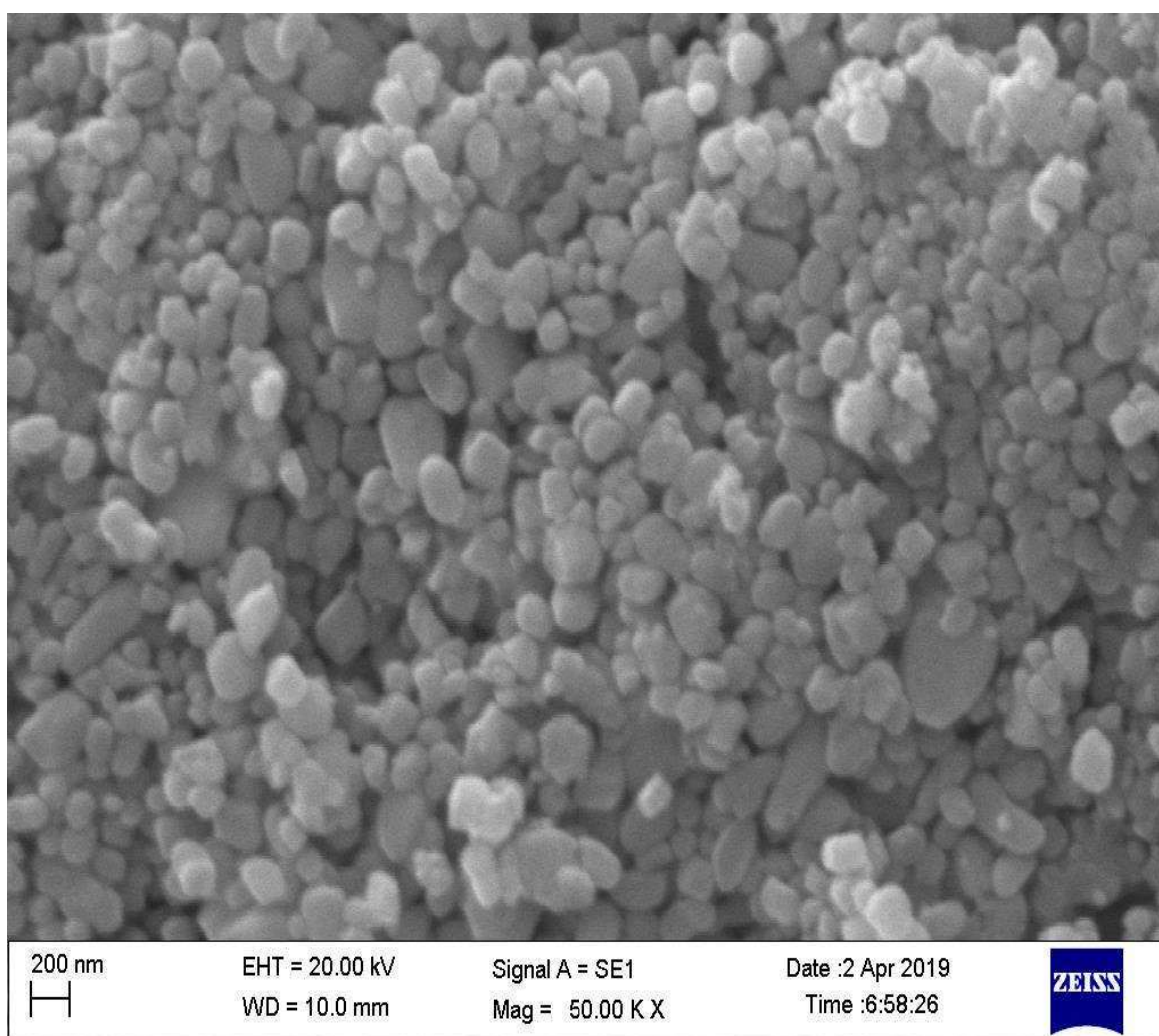


Figure 3. SEM images of Bi₂Fe₄O₉ ceramic sintered at 800°C for 8h

Microstructure feature of the grains of Bi₂Fe₄O₉ ceramic was observed in the SEM analysis on the scale 200 nm which is shown in the **Figure 3**. It is revealed from the figure that homogenous grain was distributed of the materials. The average grain size of Bi₂Fe₄O₉ ceramic was found to be 100±20 nm, measured with the help of Image- J software.

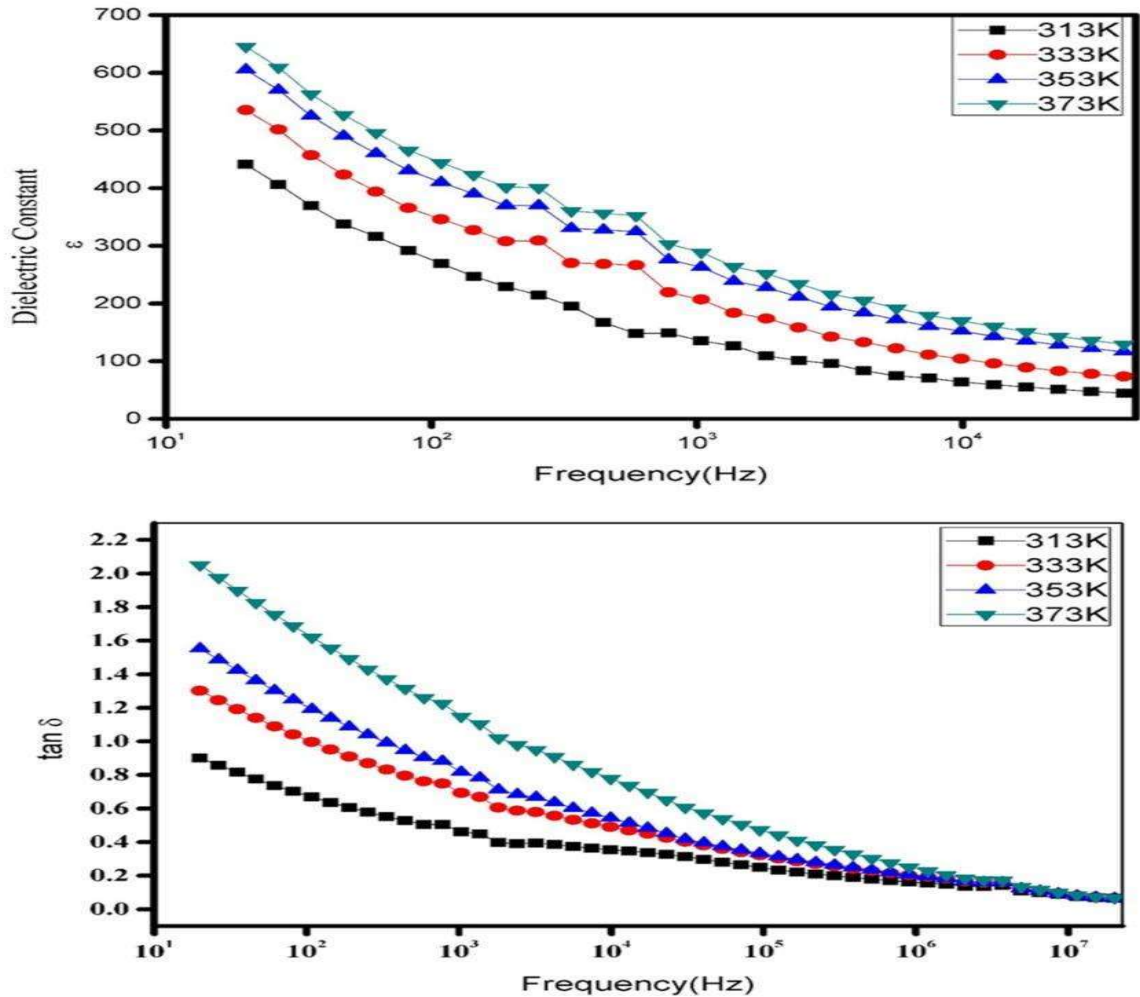


Figure 4. Variation of (a) real dielectric constant (ϵ'), (b) dielectric loss ($\tan \delta$) as a function of frequency at some selected temperatures.

The variation of Dielectric constant (ϵ) with frequency (Hz) and few selected temperatures of $\text{Bi}_2\text{Fe}_4\text{O}_9$ ceramic are shown in **Figure 4**. The value of ϵ decreases with increase of frequency as clear from the figure and remains constant at higher frequency range. This value at lower frequency region may be arises due to space charge polarization in between semi-conducting grains and insulating grain boundaries and

constant value of ϵ due to rapid periodic reversal of electric at higher frequency regions. That is why no charge accumulation occurs at interface in higher frequency and results lower value of ϵ . The value of dielectric constant of the material is found to be 645.45 at 20 Hz and 373K.

Plots of dielectric loss ($\tan \delta$) with frequency at different temperatures of Bi₂Fe₄O₉ ceramic is shown in **Figure 4**. It is clearly revealed from the figure that the same trends in $\tan \delta$ with frequency is observed as the dielectric constant up to 100 kHz and after which above 100 kHz, the value of dielectric loss exactly merged to each other over all measured temperatures. The value of $\tan \delta$ for Bi₂Fe₄O₉ ceramic was found to be less than 1.0 at 1 kHz at all measured temperatures. The higher value of dielectric loss of Bi₂Fe₄O₉ ceramic may be due to space charge polarization.

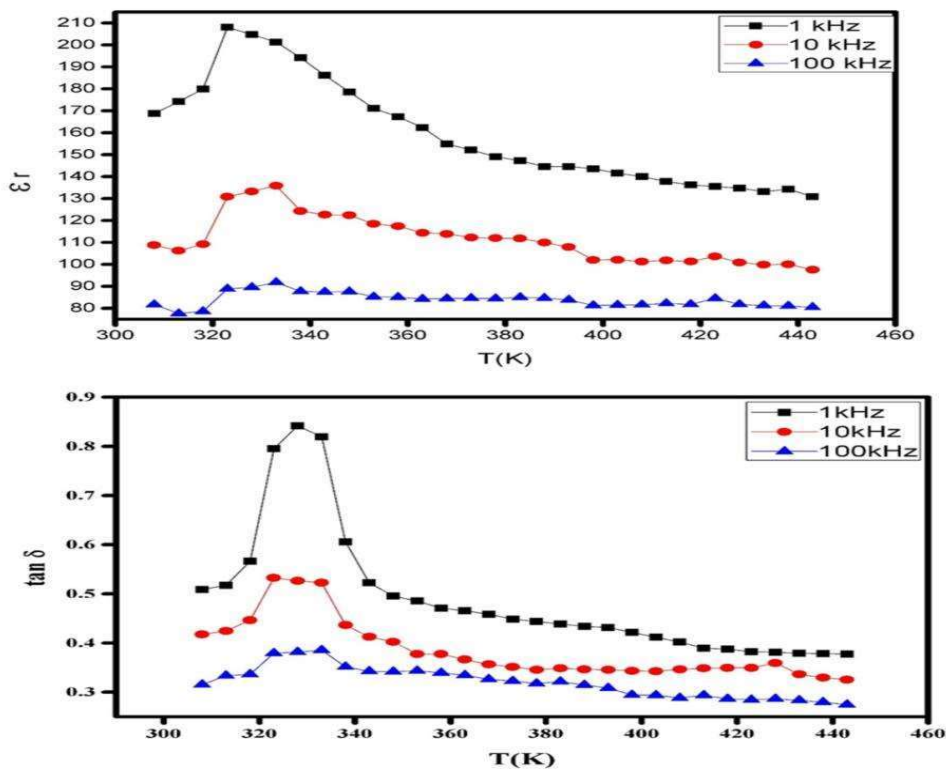


Figure 5. Temperature dependence (a) dielectric constant (ϵ'), (b) dielectric loss ($\tan \delta$) at a few selected frequencies

Figure 5 shows the variation of relative permittivity with temperature at some particular frequencies of Bi₂Fe₄O₉ ceramic. The above figure shows that dielectric constant first increases and attain maxima and then decreases with increase of temperature.

The increment of ϵ with decreasing frequency may be due to reduction of bonding force in between the atoms which enhance the polarization of the materials. The value of dielectric constant for Bi₂Fe₄O₉ at 1 kHz, 10 kHz and 100 kHz were found to be 209, 138, and 88 respectively. The plot of Dielectric loss ($\tan \delta$) with temperature at 1 Hz, 10 Hz and 100 kHz is shown in **Figure 5**. The dielectric loss first increases and then decreases with increasing temperature. The increase in the $\tan \delta$ with temperature may be regarded as oxygen vacancy present in the BiFeO₃ ceramic during sintering process. The value of $\tan \delta$ for Bi₂Fe₄O₉ was found to be 0.87, 0.33 and 0.14 at 1 kHz, 10 kHz and 100 kHz, respectively.

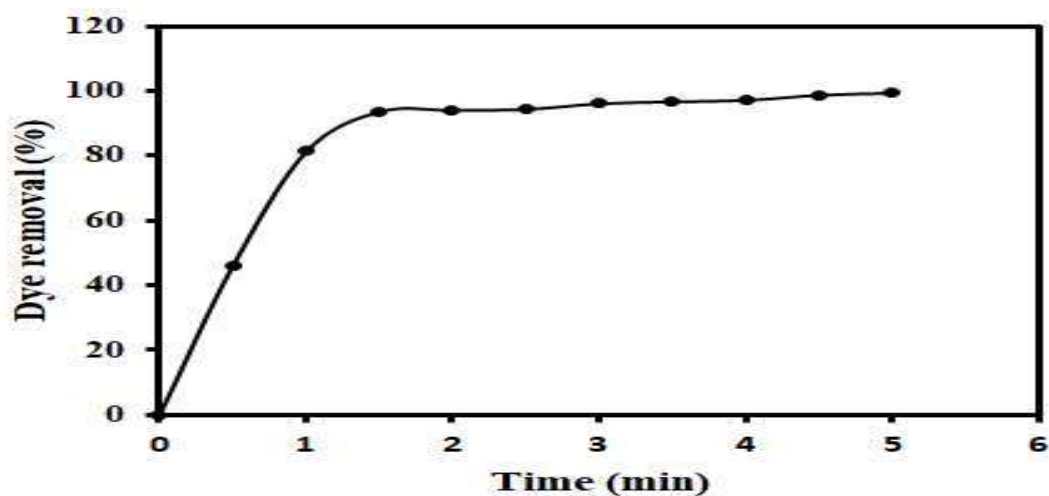


Figure 6. The effect of contact time on CR removal (%) at different concentration of CR

The contact time of dye solution with adsorbent is adversely affects the dye removal efficiency [19]. It is helpful to analyze the kinetics of dye removal. The effect of process time with respect to Congo Red (CR) removal (%) by $\text{Bi}_2\text{Fe}_4\text{O}_9$ under the following conditions (pH: 7.0, CR concentration: 20 mg/L, adsorbent dose, 0.1 g/L, temperature: 30 ± 1.0 °C, and 120 rpm) is shown in **Figure 6**. The removal efficiency of CR dye was very fast up to 1.5 min and thereafter reached to the state of equilibrium after a very short contact time (5.0 min). Initially, 93.5% of CR removal efficiency was obtained in 1.5, which further increased with process time and reached 99.3% in 5 min. The obtained result reveals that the material offers very rapid adsorption of CR dye on $\text{Bi}_2\text{Fe}_4\text{O}_9$. The effective adsorption of CR dye by $\text{Bi}_2\text{Fe}_4\text{O}_9$ was endorsed to its higher surface area and more available surface active sites for adsorption of Cr dye.

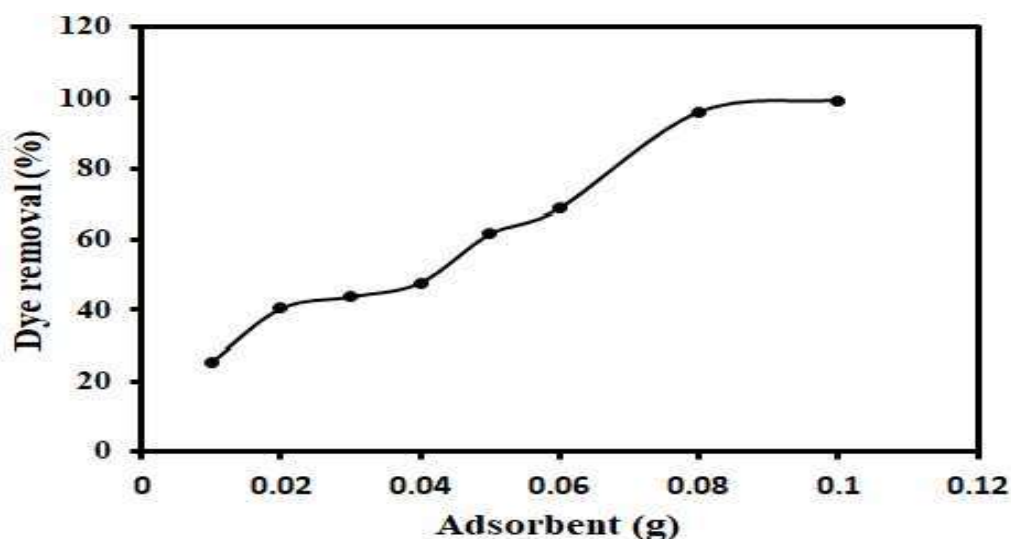


Figure 7. The effect of adsorbent dose (g) on the removal (%) of CR

Effect of process time on CR removal efficiency by $\text{Bi}_2\text{Fe}_4\text{O}_9$ (pH: 7.0, CR concentration: 20 mg/L, adsorbent dose: 0.1 g/L: temperature: 30 ± 1.0 °C, and 120 rpm) : The influence of adsorbent dose (0.1-1.0 g/L) against CR removal (%) by $\text{Bi}_2\text{Fe}_4\text{O}_9$ under following conditions (pH: 7.0, CR concentration: 20 mg/L, process time: 5.0 min, temperature: 30 ± 1.0 °C, and 120 rpm) is shown in **Figure 7**. A gradually increasing trend of CR dye removal efficiency with increasing adsorbent dose was obtained. The low amount of adsorbent provides less adsorption site at constant CR dye concentration, resulting in low removal efficiency was found. Whereas, large adsorbent dosage leads to an increase in active surface area and adsorption site at constant CR dye concentration, and thus increased CR dye removal efficiency. The CR removal efficiency of 25.4% was found with an adsorbent dose of 0.1 g/L, which was further increased to 97 % with 0.8 g/L of adsorbent dose. After that, the CR removal efficiency was not much improved with the adsorbent dose and found to be 99% with 1.0 g/L of adsorbent dose. It was probably due to about all adsorbate (i.e., CR dye) was adsorbed

onto the active sites of the adsorbent (Bi₂Fe₄O₉). The effect of adsorbent dose (i.e., polydopamine-kaolin and polydopamine- reduced graphene oxide-kaolin) on the removal of Methylene Blue (MB) was studied and high removal efficiency of MB was obtained at high adsorbent dose due to availability of high active surface area and adsorption site [19].

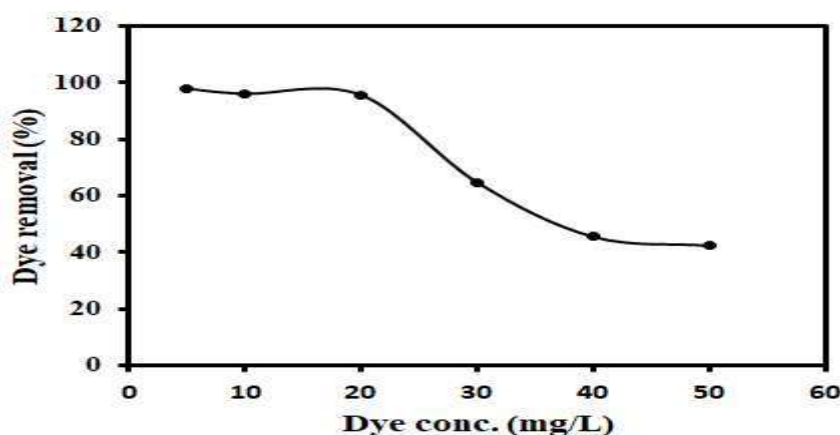


Figure 8. The effect of adsorbent dose (mg/L) on the removal (%) of CR

Figure 8 depicts Effect of adsorbent dose on CR removal efficiency by Bi₂Fe₄O₉ (pH: 7.0, CR concentration: 20 mg/L, process time: 5.0 min, temperature: 30±1.0 °C, and 120 rpm). Effect of CR concentration. The effect of initial CR concentration (5-50 mg/L) in removal efficiency (%) of CR dye by Bi₂Fe₄O₉ under following conditions (pH: 7.0, adsorbent dose: 0.1 g/L, process time: 5.0 min, temperature: 30±1.0 °C, and 120 rpm) is shown in **Figure 8**. It can be perceived from the figure that the adsorption of CR dye on Bi₂Fe₄O₉ was decreased with increasing initial concentration of CR. Initially, CR removal efficiency was gradually decreased with increasing CR up to 20 mg/L, and thereafter the CR removal efficiency was decreased very sharply with increasing CR concentration. The highest CR removal efficiency of 97.8% was obtained at the lowest CR concentration of 20 mg/L, whereas the lowest CR removal

efficiency of 42.5% was obtained at the highest CR concentration of 50 mg/L. The high concentration of CR dye could lead to the quick saturation of active site; hence the removal efficiency decreased at high CR concentration. The adsorption of methylene blue (MB) by graphene oxide modified kaolin was studied at various MB concentrations (5-40 mg/L), and the lowest removal efficiency of MB was obtained at the highest concentration due to saturation of active sites [20].

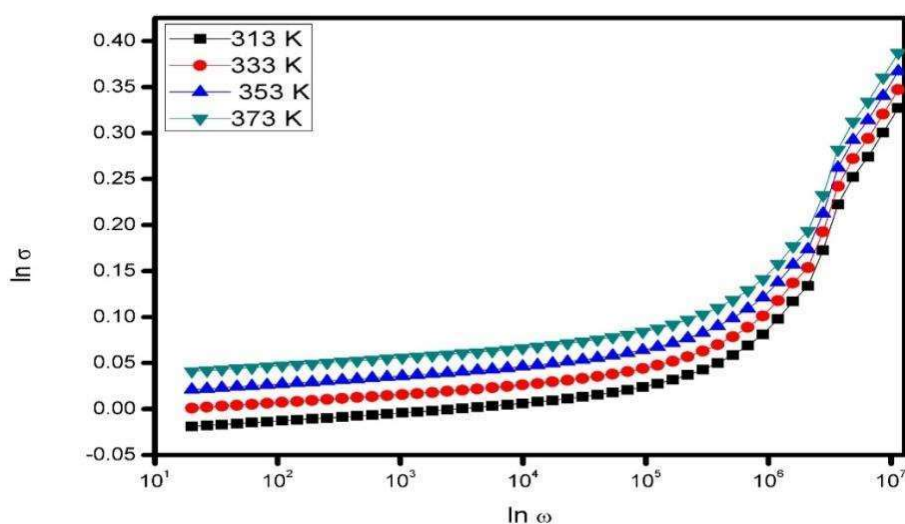


Figure 9. Conductance vs frequency graph

The conductivity behavior of Bi₂Fe₄O₉ material shows photoconductivity and optical activity for the improvement of their properties. **Figure 9** shows the frequency-dependent conductivity behavior at completely different temperatures. The electrical transport properties of the materials derived from AC conductivity and therefore the total conductivity of the materials measured through Almond–West power law that was calculated by the following equation 3. Frequency dependent of AC conductivity for Bi₂Fe₄O₉ ceramic was determined by Jonscher’s power law as given by using equation 4.

$$\sigma_{AC} = \sigma_{DC} + A\omega^s \quad (3)$$

$$\sigma_{AC} = A\omega^s \quad (4)$$

where, σ_{DC} is the frequency-independent conductivity dominant at the lower frequency region. A is the temperature-dependent pre-exponential factor and s is the frequency exponent parameters ($0 > s > 1$), dependent on both of materials and temperature and frequency independent, ω is angular frequency ($\omega = 2\pi f$). The value of frequency exponent parameters(s) obtained from the slope of the curve by linear square fitting and found to be -0.23,-0.12, 0.25 and 0.42 at 313, 333, 353 and 373 K temperatures. It is observed that the value of s for $\text{Bi}_2\text{Fe}_4\text{O}_9$ ceramic almost equal to 1 and increases with increase of temperatures. The increase in s value with temperatures indicates the presence of hopping charge conduction mechanism in the $\text{Bi}_2\text{Fe}_4\text{O}_9$ ceramic.

The activation energy for the AC conductivity, E_{ac} of $\text{Bi}_2\text{Fe}_4\text{O}_9$ ceramic sintered at 800 °C for 8 h, can be calculated from the slope of $\log \sigma_{AC}$ vs. inverse of temperature curve is depicts in the figure. It is observed from the figure that the value of conductivity linearly increases with increases of temperature. The AC conductivity was strongly correlated with the conduction mechanism in the materials over DC conductivity which occurred at higher temperature side due to thermally activated process. The temperature –dependent of AC conductivity can be measured by Arrhenius equation and it calculated with the help of following expressions

$$\sigma = \sigma_0 \exp\left(\frac{-E_a}{kT}\right) \quad (5)$$

where, σ is the conductivity of the materials, σ_0 is the pre-exponential factor, E_a is the activation energy for the thermally activated process, T is the absolute temperature and, k is the Boltzmann constant.

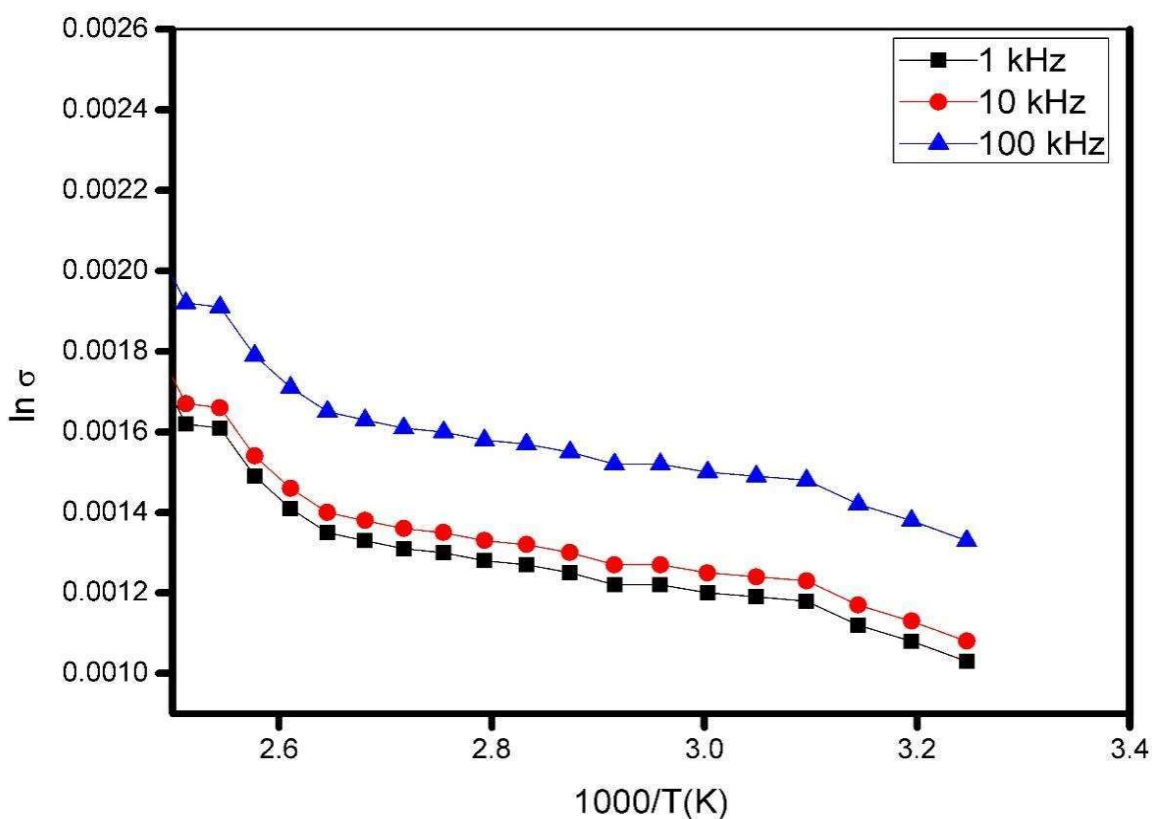


Figure.10. Conductance vs temperature graph.

The activation energy of Bi₂Fe₄O₉ sample measured by using linear fitting of **figure 10** and observed to be 0.042, 0.039 and 0.037 eV at 1 kHz, 10 kHz, and 100 kHz, respectively. From above observed data, it is found that the activation energy values (E_a) slightly increases with decreasing the frequency which may be lead to be thermally activated process. The lesser value of E_a with regarding to higher frequency may be

cause of hopping charge mechanism which increases the conduction mechanism of the materials [5].

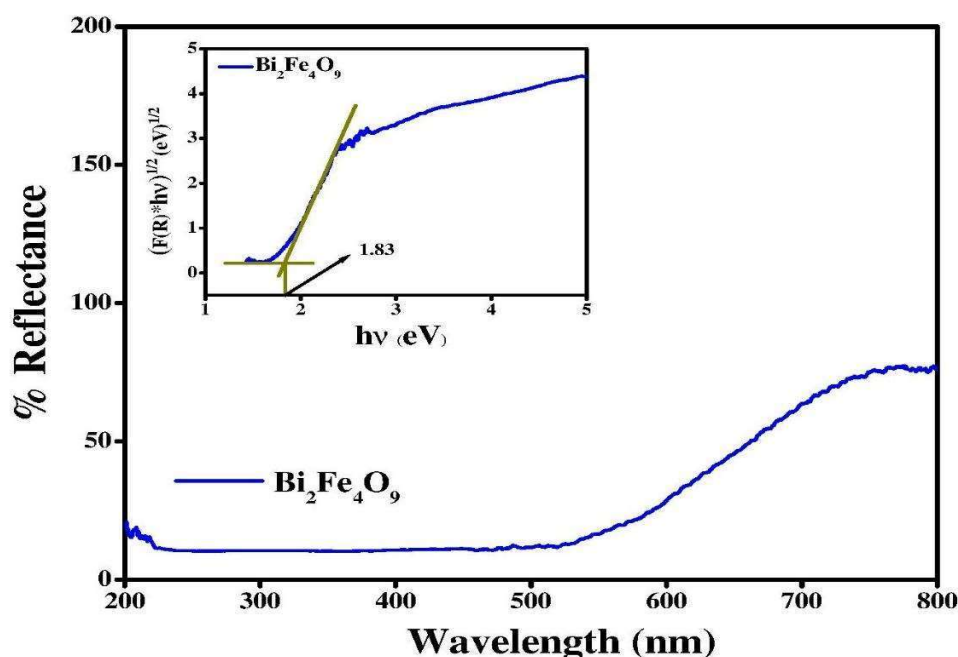


Figure.11. Diffuse reflectance spectra of Bi₂Fe₄O₉ nanoparticle. Inset figure showing optical bandgap value of Bi₂Fe₄O₉ nanoparticle evaluated from Kubelka-Munk theory.

Diffuse reflectance spectra of Bi₂Fe₄O₉ nanoparticle **Figure 11** showing strong light absorption in the UV-Visible region. However, it has also strong optical absorption extending upto NIR region. Similarly, reported optical band gap value (E_g) of Bi₂Fe₄O₉ nanoparticle is 1.29 eV [21][22], that may vary depending upon the size of nanoparticle prepared and corresponding synthesis process. Similarly variation in techniques adopted for measurement of optical band gap, also have significant effect on the measured band gap value. In the present experiment we have adopted Kubelka -Munk theory for evaluation of optical band gap value of Bi₂Fe₄O₉ nanoparticle, from recorded diffuse reflectance spectra.

$$F(R) = \frac{\alpha}{S} = \frac{(1-R)^2}{2R} \quad (7)$$

F(R): Kubelka-Munk function,

α : absorption coefficient,

R: reflectance,

S: scattering factor

Equation 7 describes that Kubelka-Munk function is proportional to absorption coefficient.

Optical band gap can be calculated from the plot of diffuse reflectance versus wavelength, where onset of linear increase in curve determines the corresponding band gap energy. Since the band gap energy. But this method of calculating band gap energy produces slightly inaccurate value, hence it is mandatory to report the type of transition (direct/indirect) during evaluation.

Absorption edge analysis was applied to find the type of transition and to determine the optical band gap represented in equation 8.

$$\alpha h\nu = k*(h\nu - E_g)^{1/n} \quad (8)$$

k: energy independent constant,

E_g: Optical band gap

The exponent n defines the type of transition where, value of n = 2 and 1/2 for direct and indirect allowed transitions respectively. Since F(R) is proportional to α , modified form of equation 2 can be represented as

$$F(R)*h\nu = k*(h\nu - E_g)^{1/n} \quad (9)$$

The exponent n in equation (3) can be determined from the plot of $(F(R).hv)^n$ vs. hv . The best fit to the straight line near the onset of absorption, observed for $n = 1/2$ recommending indirect allowed transition for Bi₂Fe₄O₉ nanoparticle.

From the plot of $(F(R)*hv)^{1/2}$ vs. hv , the band gap value of prepared Bi₂Fe₄O₉ nanoparticle is calculated to be 1.83 eV, from the extrapolation of linear region of curve.

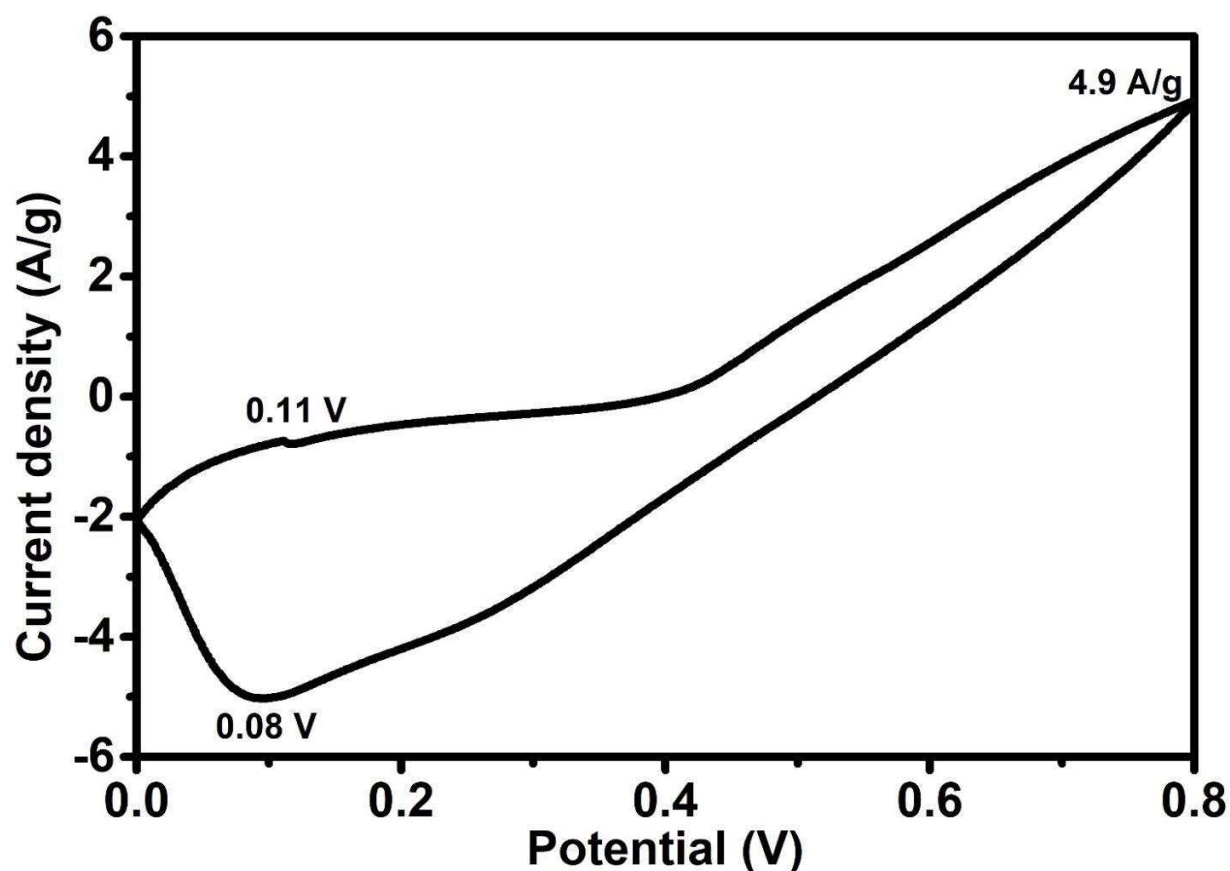


Figure 12. Cyclic voltammety of bismuth ferrite based electrode in 1M KOH at 5 mV/s

It can be seen from **figure 12** that Bi₂Fe₄O₉ has redox peaks at 0.11 V/0.08 V. This shows that the material is pseudocapacitive in nature. The maximum currents generated during the CV are 4.9 A/g and 5.1 A/g for oxidation and reduction, respectively. The calculated specific capacitance for the electrode is 215 F/g. This

signifies that the material can also be used as an electrode in electrochemical supercapacitors.

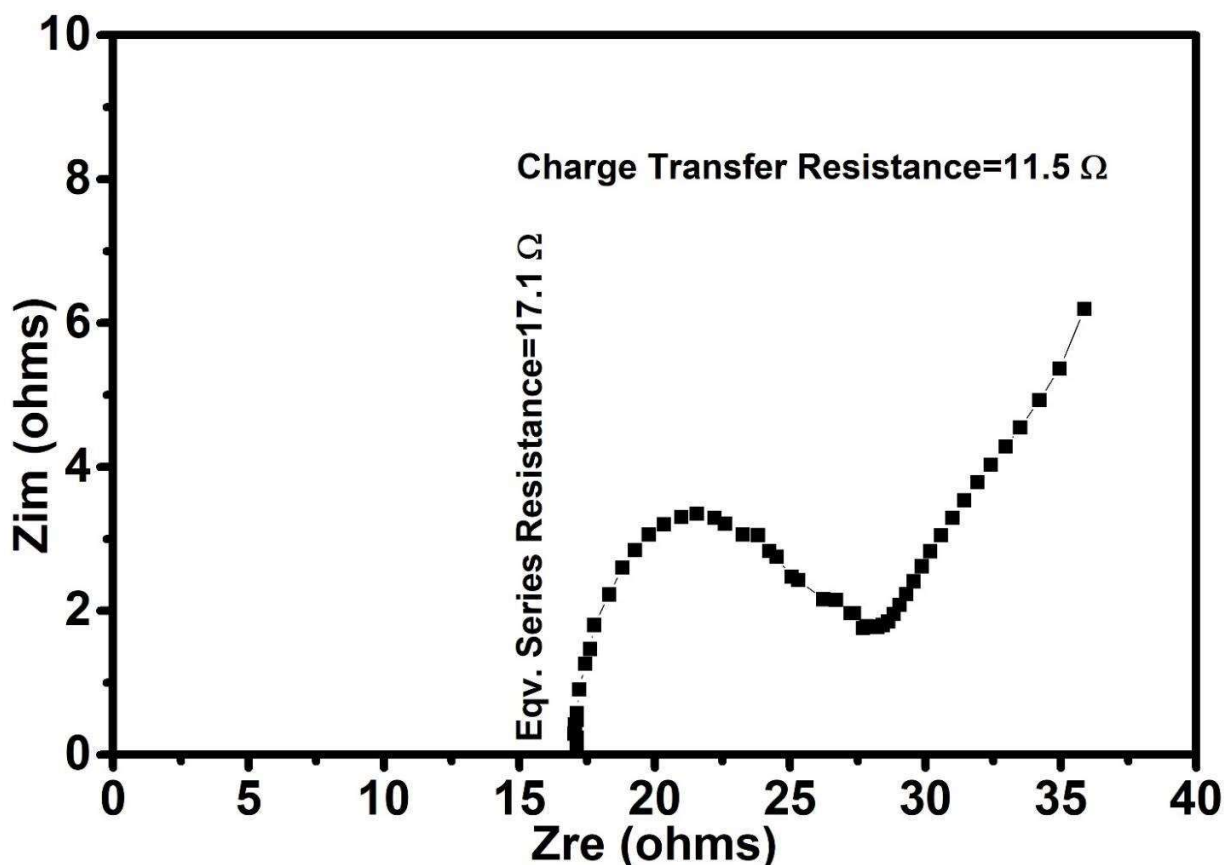


Figure. 13. Nyquist plot of bismuth ferrite based three electrode system

From **figure 13**, The equivalent series resistance is found to be 17.1 Ω and charge transfer resistance is 11.5 Ω. Due to minimum charge transfer resistance it can be used in supercapacitors as electrodes (as conducting in nature).

Conclusion

Bi₂Fe₄O₉ ceramic was synthesized by semi wet method and studied as active photocatalysts. The sample was characterized by using different characterization method such as X-ray diffraction (XRD), Scanning electron microscopy (SEM),

transmission electron microscopy (TEM). Additionally, the photocatalytic activities of three electrode system is found to be 215 F/g, and it exhibits pseudocapacitive nature. The electrode has a comparatively less charge transfer resistance of 11.5 Ω . The dielectric constant of the Bi₂Fe₄O₉ was calculated with variation temperature and frequency and found to be 645.45 at 20 Hz and 373K. synthesized Bi₂Fe₄O₉ were evaluated by photodegradation of Congo Red (CR). The Effect of process time, adsorbent dose and initial Congo Red concentration were optimized at batch mode and the outcomes demonstrate that Bi₂Fe₄O₉ shows the pre-eminent potential for the photodegradation of Congo Red. The UV-visible study of BFO revealed a direct transition at 1.8 eV for the visible light absorption. The frequency and temperature-dependent AC conductivity observed by Arrhenius equation explains the hopping charge mechanism in the Bi₂Fe₄O₉ ceramic. The expected specific capacitance of Bi₂Fe₄O₉ based

Acknowledgments

Manish Kumar Verma thanks Head, Department of Chemistry, IIT(BHU) Varanasi, India, for the continuation of financial assistance as CSIR fellowship. The authors are thankful to the Incharge, CIFC, IIT(BHU) Varanasi for providing TEM, SEM, and XRD facilities.

Conflict of Interest: The authors declare that there is no conflict among them regarding the publication of this article.

References

- [1] X. Li *et al.*, “(Bi, C and N) codoped TiO₂ nanoparticles,” *Journal of Hazardous Materials*, vol. 161, no. 1, pp. 396–401, 2008.
- [2] A. Sun, H. Chen, C. Song, F. Jiang, X. Wang, and Y. Fu, “Magnetic Bi₂₅FeO₄₀-graphene catalyst and its high visible-light photocatalytic performance,” *RSC Advances*, vol. 3, no. 13, p. 4332, 2013.
- [3] S. Z. Chu, S. Inoue, K. Wada, D. Li, H. Haneda, and S. Awatsu, “Highly porous (TiO₂-SiO₂-TeO₂)/Al₂O₃/Ti O₂ composite nanostructures on glass with enhanced photocatalysis fabricated by anodization and sol-gel process,” *Journal of Physical Chemistry B*, vol. 107, no. 27, pp. 6586–6589, 2003.
- [4] C. Y. Zhang, H. J. Sun, W. Chen, J. Zhou, B. Li, and Y. B. Wang, “Hydrothermal synthesis and photo-catalytic property of Bi₂₅FeO₄₀ powders,” *IEEE International Symposium on Applications of Ferroelectrics*, pp. 1–3, 2009.
- [5] M. K. Verma *et al.*, “Bi₂₅feo₄₀ polycrystalline ceramic as highly efficient photocatalyst synthesised via economical chemical route,” *Materials Technology*, vol. 35, no. 8, pp. 483–493, 2020.
- [6] J. Luo and P. A. Maggard, “Hydrothermal synthesis and photocatalytic activities of SrTiO₃-coated Fe₂O₃ and BiFeO₃,”

- Advanced Materials*, vol. 18, no. 4, pp. 514–517, 2006.
- [7] A. P. Finlayson, V. N. Tsaneva, L. Lyons, M. Clark, and B. A. Glowacki, “Evaluation of Bi-W-oxides for visible light photocatalysis,” *Physica Status Solidi (A) Applications and Materials Science*, vol. 203, no. 2, pp. 327–335, 2006.
- [8] N. I. Zakharchenko, “Catalytic Properties of the System Fe₂O₃-Ga₂O₃ in Ammonia Oxidation,” *Russian Journal of Applied Chemistry*, vol. 76, no. 3, pp. 399–406, 2003.
- [9] R. Qian-Jing and Z. Wei-De, “Tunable morphology of Bi₂Fe₄O₉ crystals for photocatalytic oxidation,” *Journal of Physical Chemistry C*, vol. 113, no. 10, pp. 4168–4173, 2009.
- [10] E. S. Jang, J. H. Won, S. J. Hwang, and J. H. Choy, “Fine tuning of the face orientation of ZnO crystals to optimize their photocatalytic activity,” *Advanced Materials*, vol. 18, no. 24, pp. 3309–3312, 2006.
- [11] X. Zhang, L. Bourgeois, J. Yao, H. Wang, and P. A. Webley, “Tuning the morphology of bismuth ferrite nano- And microcrystals: From sheets to fibers,” *Small*, vol. 3, no. 9, pp. 1523–1528, 2007.
- [12] Y. Xiong, M. Wu, Z. Peng, N. Jiang, and Q. Chen, “Hydrothermal synthesis and characterization of Bi₂Fe₄O₉ nanoparticles,” *Chemistry Letters*, vol. 33, no. 5, pp. 502–503, 2004.
- [13] J. T. Han *et al.*, “Tunable synthesis of bismuth ferrites with various morphologies,” *Advanced Materials*, vol. 18, no. 16, pp. 2145–2148, 2006.

- [14] K. J. D. MacKenzie, T. Dougherty, and J. Barrel, “The electronic properties of complex oxides of bismuth with the mullite structure,” *Journal of the European Ceramic Society*, vol. 28, no. 2, pp. 499–504, 2008.
- [15] T. Das and B. Verma, “Polyaniline based ternary composite with enhanced electrochemical properties and its use as supercapacitor electrodes,” *Journal of Energy Storage*, vol. 26, no. June, p. 100975, 2019.
- [16] T. Das and B. Verma, “Polyaniline-Acetylene black-Copper cobaltite based ternary hybrid material with enhanced electrochemical properties and its use in supercapacitor electrodes,” *International Journal of Energy Research*, vol. 44, no. 2, pp. 934–949, 2020.
- [17] T. Das and B. Verma, “Synthesis of polymer composite based on polyaniline-acetylene black-copper ferrite for supercapacitor electrodes,” *Polymer*, vol. 168, no. October 2018, pp. 61–69, 2019.
- [18] T. Das and B. Verma, “High performance ternary polyaniline-acetylene black-cobalt ferrite hybrid system for supercapacitor electrodes,” *Synthetic Metals*, vol. 251, no. March, pp. 65–74, 2019.
- [19] K. He *et al.*, “Graphene hybridized polydopamine-kaolin composite as effective adsorbent for methylene blue removal,” *Composites Part B*, vol. 161, no. August 2018, pp. 141–149, 2019.
- [20] K. He *et al.*, “Journal of the Taiwan Institute of Chemical Engineers Enhanced removal performance for methylene blue by kaolin with graphene oxide modification,” *Journal of the Taiwan Institute of Chemical Engineers*, vol. 89, pp. 77–85, 2018.

- [21] C. Deng *et al.*, “Synthesis of sillenite-type Bi₃₆Fe₂O₅₇ and elemental bismuth with visible-light photocatalytic activity for water treatment,” *Frontiers of Materials Science*, vol. 12, no. 4, pp. 415–425, 2018.
- [22] Y. Zhang *et al.*, “Photoelectrochemical response and electronic structure analysis of mono-dispersed cuboid-shaped Bi₂Fe₄O₉ crystals with near-infrared absorption,” *RSC Advances*, vol. 4, no. 54, pp. 28209–28218, 2014.